Compressive behavior of Body-Centered-Cubic (BCC)-like ultra-lightweight Carbon Fiber Reinforced Polymer (CFRP) lattice-based sandwich structures

Pablo Vitale [a,*], Joaquin Montero [b], Gaston Francucci [c], Helmut Rapp [a], Kristin Paetzold [d], Ariel Stocchi [c], Philipp Höfer [a]

[a] *Institute of Lightweight Engineering, Universität der Bundeswehr München, Neubiberg, Germany*
[b] *Boeing Research & Technology, Structural Technologies, Munich, Germany*
[c] *Structural Composites Group (CET), Research Institute of Material Science and Technology, INTEMA-CONICET, Mar del Plata, Argentina*
[d] *Institute of Machine Elements and Machine Design, Technische Universität Dresden, Dresden, Germany*

ARTICLE INFO

ABSTRACT

3D lattice structures comprise a connected network of segments that allow positioning of the base material where needed while maintaining an open-cell characteristic. These structures represent an ideal lightweight core material for high-performance sandwich panels. This work presents, for the first time, the performance of lattice-based cores fabricated via indirect additive manufacturing using pultruded Carbon Fiber Reinforced Polymer (CFRP) rods. The CFRP sandwich panels were tested under out-of-plane compression, and their compressive properties and failure modes were predicted via analytical and FE analyses, later contrasted with mechanical testing. Finally, the study compares favorably with similar core materials found in the literature.

1. Introduction

For several years now, lattice-like structures have been developed as an alternative to different cellular topologies, such as honeycomb cores [14] for producing lighter and stronger open-structured materials. Lattice materials were originally based on metals such as aluminum or titanium alloys [14,19], but they are also found based on ceramics [38] or polymers [15]. Lately, lattice materials are gradually becoming CFRP-based materials [9,32], taking advantage of their high strength-to-weight and high stiffness-to-weight ratios. A commonly used unit cell for lattice structures is the Body-Centered Cubic (BCC) due to its simplicity and similar or better mechanical properties compared to conventional honeycomb cores [16]. Smith et al. [25,26] studied the compressive behavior of BCC and BCC-Z. In their study, employing metallic laser-based Powder Bed Fusion (PBF-LB/M) of 316L stainless-steel, different 3D cores were obtained with relative densities $\bar{\rho}$ ranging from 3.5 % to 13.9 % (i.e., 280 kgm^{-3} to 1112 kgm^{-3}, in absolute values) for the BCC presenting elastic moduli ranging from 10.6 MPa to 207.5 MPa. Zhang et al. [37,38] studied Cellular Ceramic Structures (CCSs) based on several structural configurations such as BCC and modified BCC (MBCC. The CCSs were fabricated from an Al$_2$O$_3$ photosensitive slurry by a Digital Light Processing (DLP) system. The

authors reported that CCSs materials performed properly showing good load-bearing capacity, and good energy absorption ability compared to similar bulk materials.

High-performance applications require the use of high-performance materials, such as CFRP. These materials have been recently used for manufacturing pyramidal lattice structures (i.e., considering only half of a BCC unit cell) from machined laminates [9]. Lattice cores based on pyramidal truss structures made from unidirectional carbon/epoxy pre-pregs oriented at [0/90]° and processed by hot-press compression molding were studied by Xiong et al. [34,35]. They reported relative core densities ranging from 1.2 % to 4.7 % (i.e., 19.37 kgm^{-3} to 72.85 kgm^{-3}) for different numbers of prepreg plies used and evaluated in out-of-plane compressive tests. They found that the core moduli fell in the range of 45.8 MPa to 241 MPa, depending on the core density. Moreover, CFRP octet-truss structures (i.e., the unit cell presents two opposite pyramidal lattices connected by its bases and not by its tops like in BCC-based) were obtained by Dong and Wadley [8] by using snap-fit nodes. They achieved relative core densities of 1.7 % to 16 % (i.e., 24.48kgm^{-3} to 230.4 kgm^{-3}), reaching peak out-of-plane elastic modulus in the range of 75 MPa to 983 MPa and compressive strengths of 0.6 MPa to 9.89 MPa.

Pyramidal truss [10] and octet truss structures [4] using resin-impregnated carbon fiber stitched yarns as base materials are

---

* Corresponding author at: Institute of Lightweight Engineering, Universität der Bundeswehr München, Werner-Heisenberg-Weg 39, Neubiberg, Germany.
E-mail address: pablo.vitale@unibw.de (P. Vitale).

Nomenclature

α	horizontal director angle
$\bar{\rho}_c$	core relative density
δ	displacement
ε_c	unit cell strain
ω	vertical director angle
ρ_c	core absolute density
ρ_s	absolute density
σ_{cB}	core compressive buckling strength
σ_{cR}	core compressive fracture strength
σ_{cpk}	core peak compressive strength
Ø or d	rod diameter
φ_f	fiber volume content
A_{cell}	cross-sectional area of a unit cell
E_{1s}	elastic modulus
E_{rod1s}	rod elastic modulus
$I_{x'}$	second moment of inertia
E_c	core out-of-plane compressive modulus
F	applied force
G_{12s}	shear elastic modulus
H	unit cell height
k	Euler buckling coefficient
L	unit cell length
l	rod length
P	applied total force
R_{1s}^-	compressive strength
R_{12s}	shear strength
s	slope
s	suffix for base material
ν_{12s}	Poisson's modulus
V_{cell}	volume of a unit cell
W	unit cell width

Table 1
Mechanical properties of the CFRP rods employed for calculations. (*) Values from data sheet.

Component	φ_f [%]	E_{1s} [GPa]	G_{12s} [GPa]	ν_{12s} [–]	ν_{12s} [–]	R_{1s}^- [MPa]	R_{12s} [MPa]
Rods	65*	115*	5.8	0.016	0.25	450*	90*
Skins	55	67.78	4.06	0.028	0.028	527.44	110

almost comparable in compression performance to other similar commercial cores, although their expected maximum mechanical potential is not reached, since the trusses present geometrical in-homogeneity along their profile. Therefore, curvatures close to the nodes negatively affect the load transmission, causing additional bending moments at the nodes instead of transmitting the load axially through the trusses from the upper to the lower skin. These disadvantages can be overcome by using new manufacturing methods employing alternative base materials to generate similar but higher-performance structures like those presented in this paper.

2. Materials and design

2.1. Materials

A design comprising BCC-like lattice structures was used for the core, giving an array of pultruded CFRP rods [28] (*T300* CF/epoxy) of density 1.55 gcm^{-3} and fiber volume content of 65 %. Three different design variants were considered with different rod diameters: 0.5 mm, 1 mm, and 1.5 mm. The sandwich skins consisted of four layers of woven *Torayca® T300-3k* [30] carbon fiber 2/2 twill fabrics, combined with epoxy resin and hardener type *L* [21]. The resulting CFRP skins have a thickness of $t = 0.80 \pm 5$ mm, an average fiber volume content of 55 %, and a density of 1.422 gcm^{-3}. The physical properties were determined experimentally. Table 1 shows the CFRP rods data employed for calculations [28], and the skins' mechanical properties pre-estimated according to the Classical Laminate Theory.

2.2. Manufacturing process

The method for obtaining sandwich panels combines different known techniques, mainly fused filament fabrication (FFF) and vacuum infusion (VI). The manufacturing of lattice cores is satisfied while correctly maintaining the desired shape, positioning, and angles involved, with good finishing quality and repeatability. A complete
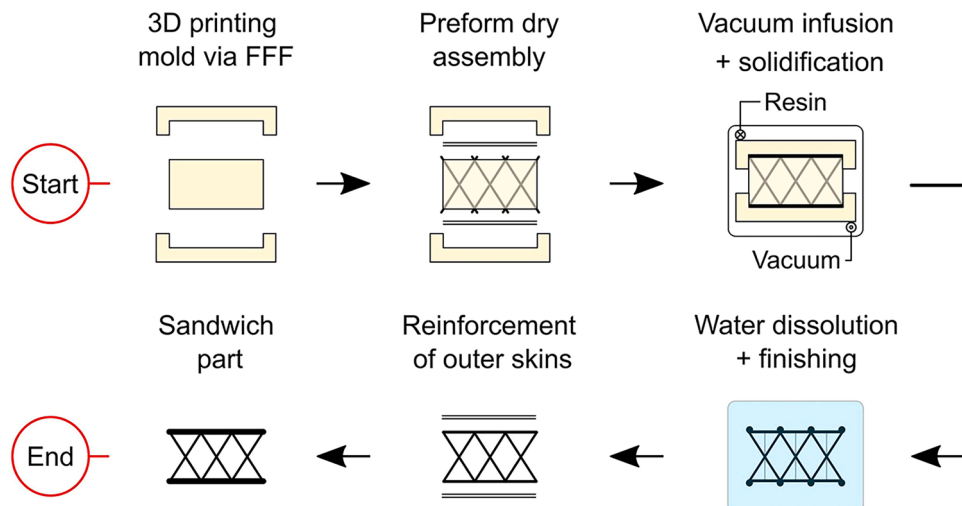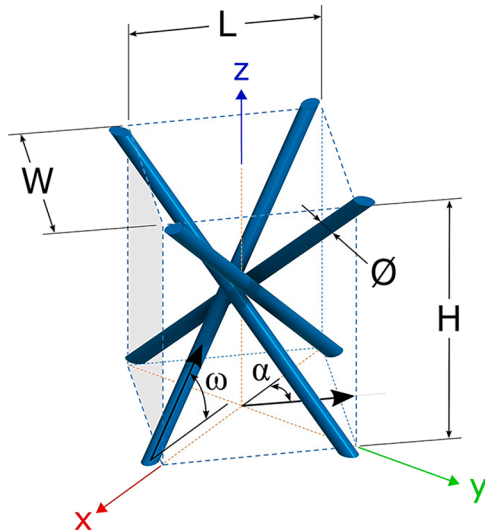

Fig. 1. Manufacturing process schematic.

Fig. 2. Parameters of the BCC-like unit cell.

Table 2
Dimensions of unit cells and core densities. (*) Predicted. (**) Own measurement.

Ø [mm]	L [mm]	W [mm]	H [mm]	α [°]	ω [°]	ρ_c^* [kgm^{-3}]	ρ_c^{**} [kgm^{-3}]
0.50	17.96	17.96	25.40	45	45	5.34	8.66
1	17.96	17.96	25.40	45	45	21.34	22.92
1.50	17.96	17.96	25.40	45	45	48.03	49.76

monolithic sandwich panel is obtained. Further details are given in the author's previous work [17].

A schematic chart of the method is summarized in Fig. 1. Soluble support structures were 3D printed via FFF that served as a fixation for the rods that form the sandwich core's lattice structure. Filaments of Polyvinyl alcohol (PVA) were employed, which dissolved completely in water leaving no trace in the CFRP matrix [18]. The dry preform was assembled using the above-mentioned base materials. After, the sandwich panel (comprising the support structure, the rods, and the sandwich skins) was manufactured by the traditional vacuum infusion technique. Finally, the support structure was dissolved in water with little finishing (e.g., removing the resin channels). If applicable, more CF layers can be attached to the outer skins to avoid rod pull-out, giving place to the final sandwich part.

2.3. Lattice core design

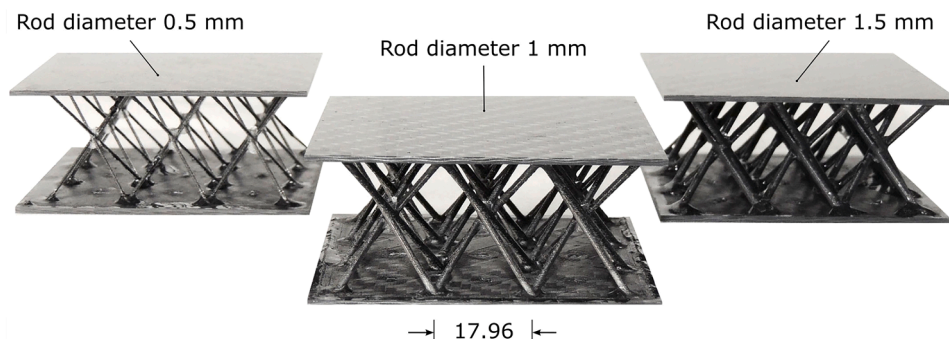Lattices depend upon three main factors: the raw materials, the grade of connectivity, and the shape of the elongated profile (e.g., rods, bars, beams, or sheets). They define the core's mechanical and physical properties. In BCC lattice structures, the rods have a connection node at the middle of the unit cell similar to a *3D-Kagome'* structure [32] but with four rods (Fig. 2). The connection mid-node is designed in a way that all the trusses meet each other at the mid-plane of the unit cell but avoid the common point while displacing the rods from the geometrical center. The connection points grant the proper support since the 3D printed mold provides in its conception, resin cavities like spheres that act as connecting nodes encompassing and holding the rods. The BCC-like design allows higher densification of the unit cell for smaller cell sizes and 45° orientation angles, a clear difference when compared to pyramid-like cells which present bigger unit cells for the same angles [9].

The parameterized unit cell design for the positioning of the rods is defined by variables such as Ø, ω, and H (Fig. 2). Three different rod diameters 0.5 mm, 1 mm, and 1.5 mm are used for studying the behavior of different core densities, and the unit cell size is maintained constant. Table 2 summarizes the unit cell's main dimensions and core densities attained. The predicted core density ρ_c is calculated within the next section. The measured core density presents few discrepancies from the prediction, attributed to the added weight incorporated by the resin-glued connections among the rods, and to the skins. The angles α and ω are 45°, H is fixed to 25.4 mm, while W and L are proposed to be equal and dependent on the core height H as $L = W = \frac{\sqrt{2}}{2}H$, resulting in a unit cell size of 17.96 mm. The samples obtained are shown in Fig. 3. The nominal dimensions are 65 mm by 65mm by 27mm, consisting of arrays of 3×3 cells.

2.4. Core relative density

The geometrical dimensions involved in the design are required to first predict ρ_c and $\bar{\rho}_c$, and then to obtain the mechanical properties of cores. The geometry of the unit cell is influenced by angles α and ω, and the length l. The latter could be also indirectly obtained by the cell height (i.e., core thickness). The expression for the cross-sectional area is given in Eq. (1). The height is defined in Eq. (2) while the cell volume is obtained in Eq.(3).

$$A_{cell} = LW = (2l\cos\omega)^2\cos\alpha\sin\alpha \tag{1}$$

$$H = 2l\sin\omega \tag{2}$$

$$V_{cell} = 4l^3\cos^2\omega \, \sin\omega\sin2\alpha \tag{3}$$

Furthermore, considering that the CFRP rods have a circular cross-section of diameter d, it is possible to obtain the average volume of the rods V_{rod} while multiplying its cross-area and the length $2l$ within a cell. Then, the relative density of the cell $\bar{\rho}_c$ and thus, the core, is obtained as Eq. (4).
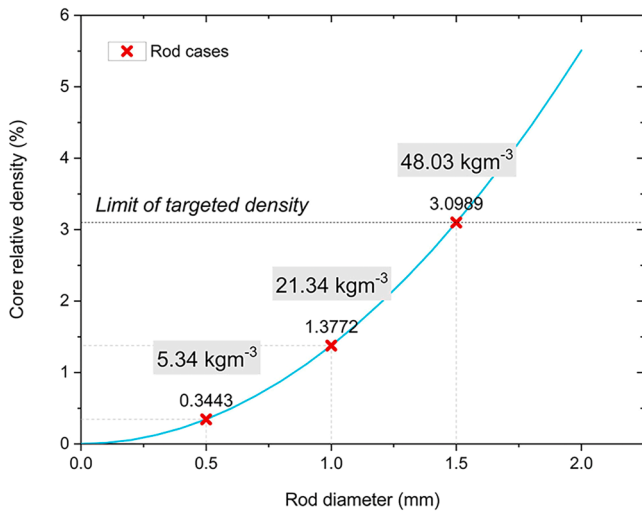

Fig. 3. Indirect additively manufactured compressive test samples.

Fig. 4. Core relative density variation as a function of the rod's diameter.

$$\bar{\rho}_c = \frac{4V_{rod}}{V_{cell}} = \frac{\pi d^2}{2l^2\cos^2\omega\sin\omega\sin2\alpha} = \frac{2\pi d^2\sin\omega}{H^2\cos^2\omega\sin2\alpha} \quad (4)$$

The variation of the relative density (Eq. 4) as a function of the diameter of the rods is shown graphically in Fig. 4, in which a quadratic polynomial curve is represented. By multiplying the relative density of the core $\bar{\rho}_c$ by the density of the rods $\rho_s = 1550$ kgm^{-3} (i.e., the base

material from which they are made), the core density is attained as $\rho_c = \bar{\rho}_c \cdot \rho_s$ (absolute values shown in the grey boxes). A targeted density below 48 kgm^{-3} is intended (i.e., the cores may be categorized as ultra-lightweight materials [20]).

3. Analytical and numerical models

Analytical and FE models were developed to predict the core mechanical response to out-of-plane compressive loading. The work is limited to simple and conventional FE methods targeting a complement for the first analytical insights about the features of the cores proposed. The single unit-cell model from Fig. 5a was taken as a base for the study. A generic compressive load was applied according to the *z*-direction to study the displacements experienced by the rods, modeled as built-in trusses at both ends. Analytical models were based on the load's decomposition into its perpendicular components upon a single rod, following a local coordinate system (Fig. 5b). The displacements were evaluated at the middle of the unit cell, taking advantage of its symmetry. The energy method applied for analyses is familiar to references [4,10,32], although with dissimilar parameters, assumptions, and specified backgrounds. Two main failure modes are identified as strength failure and stabilization failure. The commercial code FEMAP™ 11.3 with NX™ Nastran® [23] was used to carry out simulations to test separately the above-mentioned failure cases. The materials were modeled using the properties listed in Table 1. The CFRP rods were simulated by discretization of 48 elements per rod, using CBAR elements.
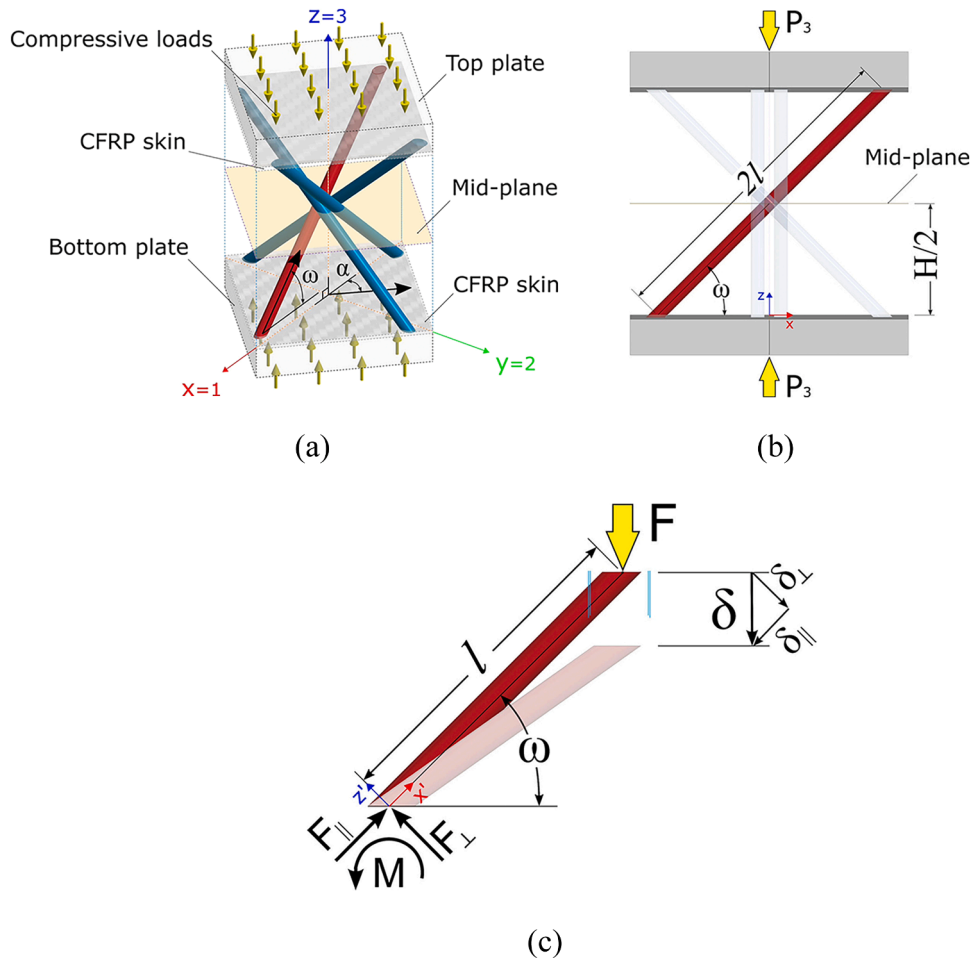

Fig. 5. Different sketches of the loading case analysed. (a) A schematic BCC-like unit cell under compressive loads. (b) Load case in the xz-plane. (c) Free body diagram of a half rod.
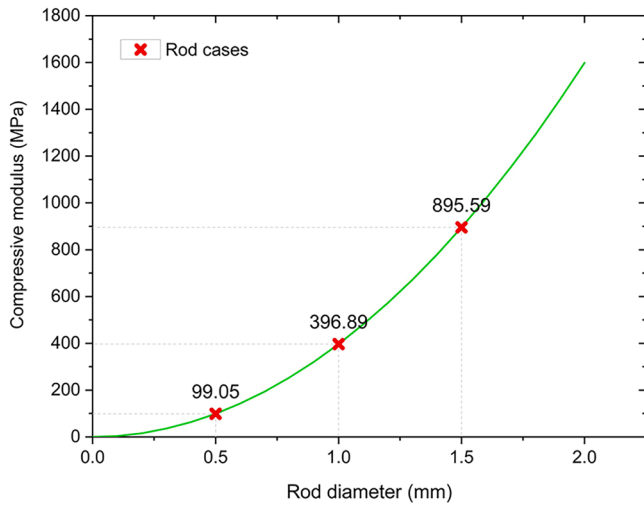
Fig. 6. Core compressive modulus predicted by the analytical model.

3.1. Compressive stiffness

The elastic straining of a single truss within half of a unit cell (Fig. 5c) is used for calculating the core compressive elastic modulus E_c. Such deformations are obtained by simple beam theory while considering the displacement δ experimented by a rod due to ¼ of the total load P.

3.1.1. Analytical approach

The total compressive stress over a unit cell is given as Eq. (5), specifying the force P by its components according to z-direction (Fig. 5). The out-of-plane compressive modulus of the core E_c can be calculated from the unit cell modulus as Eq. (6).

$$\sigma_c = \frac{P}{A_{cell}} \equiv \frac{2(|F_\parallel|\sin\omega + |F_\perp|\cos\omega)}{(l\cos\omega)^2\sin2\alpha}$$

$$= E_{rod1s}\frac{\pi d^2\delta}{2l^3\cos^2\omega\sin2\alpha}\left[\sin^2\omega + \frac{3}{4}\left(\frac{d}{l}\right)^2\cos^2\omega\right] \tag{5}$$

$$E_c \approx E_{rod1s}\frac{\pi d^2\sin^3\omega}{2l^2\cos^2\omega\sin2\alpha} \tag{6}$$

The variation of the compressive modulus with the rod diameter is shown in Fig. 6. The elastic modulus of the core depends directly on the rod diameter, following a parabolic function. A detailed mathematical analysis deriving the above-mentioned equations is provided in the Appendix.

3.1.2. Numerical approach

Simulations were carried out to have better insights into the unit cell lattice structure behavior:

1. Simulating a BCC-like structure representing the effect of mid-plane connecting points as an array of bars (see Fig. 7).
2. Simulating an equivalent traditional BCC structure via two different boundary conditions set at the mid-plane as a pinned node or as a node with rotational constraints.

The first case emulates the glue contact among the rods. The end nodes of the array of bars on the mid-plane (i.e., the magenta-colored bars in Fig. 7c) are merged with the corresponding nodes of the main support rods. In addition, this simulation model aimed to evaluate the resultant forces over the mid-plane node by complementary studies (not shown in this work). In these complementary studies, a possible rupture of the middle connection of the rods was also considered, calculating the resultant forces/stresses over the mid-plane array of bars, distinguishing the compression loads and the shear loads, and comparing them to the maximum admissible load/stress of the glue. Different bar rigidities on the mid-plane array were employed to evaluate their effect on the mid-plane node behavior. Two further load cases were simulated as 1 kN and 10 kN forces applied on the top of the unit cell (refer to Fig. 5), employing both linear and non-linear FE simulations. As a partial conclusion, it was found that the unit cell members shall fail before the mid-plane node bar array fails, in which the stresses were seen to be smaller than the admissible stress of the glue.

In cases 1. and 2., each end of the rods is fully constrained, and the mid-plane connecting point is free to displace over z-direction. Here, only the lattice with rod diameter d = 0.5 mm is shown as an example for analysis. The results of the linear static simulated strains obtained for a total generic load of 1 kN over the z-axis at the top-end nodes were 3.1306 % for the BCC-like case, and 3.1312 % for the BCC case. This represents a difference of 0.02 %, meaning that there are no substantial differences in terms of displacements if the simulations are carried out
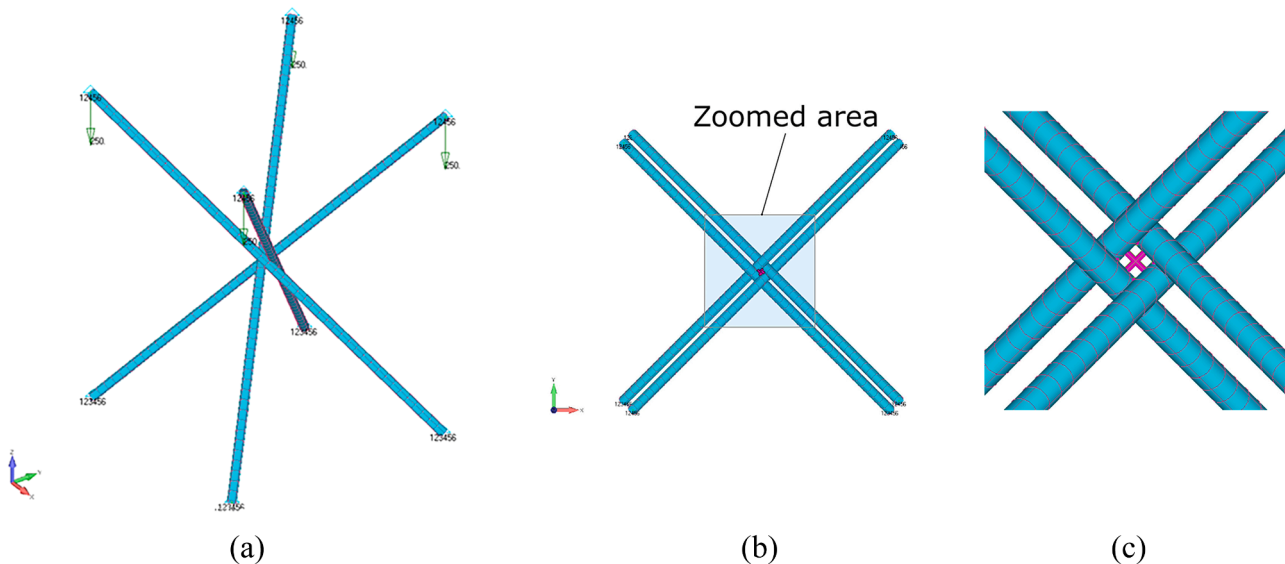

Fig. 7. Bar-array FE renders of the unit cell employed for the simulation comparison. (a) BCC-like unit cell (isometric). (b) BCC-like unit cell (top). (c) Detail of central node as an array of bars.

Table 3
Core compressive elastic moduli predicted by FE. (*) Theoretical value for comparison.

Ø [mm]	L [mm]	H [mm]	δ [mm]	s [N mm^{-1}]	ε_c [µm m^{-1}]	E_c [MPa]	E_c^* [MPa]
0.50	17.96	25.40	0.782	1274.06	3079.82	100.65	99.05
1	17.96	25.40	0.195	5123.58	767.38	403.95	396.89
1.50	17.96	25.40	0.087	11,547.37	340.94	909.19	895.59

either as BCC or BCC-like unit cell models and the corresponding cell mechanical properties are assumed as equivalent. The rotational constraints at the central node presented no remarkable effects in terms of total displacements.

To further complement the analytical compressive modeling, linear static finite element simulations were implemented for predicting the elastic modulus E_c, considering the three different rod diameters proposed. Thus, the E_c of BCC-like cores are based on the slope $s = \frac{P}{\delta}$ and calculated by Eq. (7), regarding H and δ at the top nodes.

$$E_c = \frac{H}{\delta}\sigma_c = \frac{H}{\delta}\frac{P}{A_{cell}} = \frac{sH}{A_{cell}} \qquad (7)$$

Table 3 shows a summary of the linear static results with a brief comparison with the theoretical results. The predicted strain was larger for the smaller diameters and thus, the core moduli vary directly proportional to the rod size. Then, the core compressive moduli were predicted as 100.65 MPa, 403.95 MPa, and 909.2 MPa, for the 0.5 mm, 1 mm, and 1.5 mm rod diameters, respectively. Good correspondence is found in the theory.

3.2. Compressive strength

The analytical and FE studies of BCC-like cover the main core failure loads and mechanisms as well. Thus, failure modes were considered when a unit cell member collapses, such as:

1. Elastic buckling of a truss, σ_{cB}
2. Compressive fracture of a truss, σ_{cR}.

$$\sigma_{cpk} = min(\sigma_{cB}, \ \sigma_{cR}) \qquad (8)$$

The governing failure mode is associated with the one that shows the lowest core peak compressive strength (Eq. (8)).

3.2.1. Analytical approach

To ease the analyses, the transversal load was neglected in the analytical calculations, as its contribution is almost negligible as detailed in the Appendix. The different failure mechanisms are described as follows.

3.2.1.1. Elastic buckling of a truss. Slender CFRP rods under compressive loads might undergo Euler buckling. Assuming that the rods are thought of as beams with two ends built in between the core and face sheets. Only half of the unit cell is employed for analyses.

$$F_{rodEu} = \frac{\pi^2 E_{rod1s} I_{x'}}{(kl)^2} \geq F_\parallel \qquad (9)$$

Euler's critical load is given as Eq. (9) [11]. Factor k presents different values according to the established boundary conditions. It shall be noted that $k = 1$, represents a truss with one end clamped and the other free, while $k = 0.5$. Then, the k values can be found between these two values ($0.5 \leq k \leq 1$) since the connections in the real case between rods and rod-skins are elastic links. In this work, as a starting point for studies is assumed that the trusses are pinned but guided at the mid-plane considering the connecting node effect. This leads to a k value
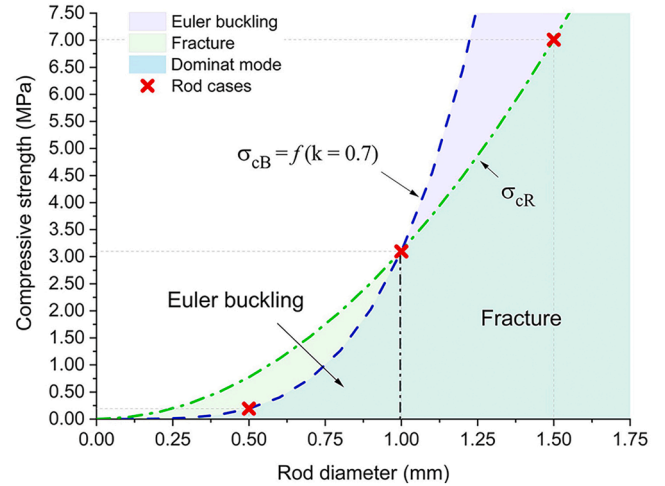

Fig. 8. Failure maps according to analytical predictions for compressive loads.

of $0.699 \approx 0.7$. This value will be later confirmed by simulations. The compressive load applied to the unit cell is decomposed to its rod members using ω and α. When the critical buckling load is attained, the parallel load $F_\parallel$ is equal in modulus to F_{rodEu}. Thus, by replacing Eq. (9) with Eq. (5) and considering the four trusses of a unit cell, the nominal compressive buckling strength of the core is given by Eq. (10).

$$\sigma_{cB} \approx \frac{E_{rod1s}\pi^3 d^4}{32k^2 l^4 \cos^2\omega \sin 2\alpha}\sin\omega \qquad (10)$$

3.2.1.2. Compressive fracture of a truss. The nominal out-of-plane compressive strength of the BCC-like CFRP core (σ_{cR}) depends upon the failure compressive strength value of the employed rod members (R_{1s}^-). The load is decomposed to the rods as a local axial stress to rods as σ_{1s}^-. Then, the fracture of the rod is attained when $\sigma_{1s}^- \geq R_{1s}^-$, and as a result, the collapse of the core. The failure load of the CFRP rods is set by Eq. (11).

$$F_{rodR} = R_{1s}^- A_{rod} \geq F_\parallel \qquad (11)$$

Recalling the previous outcome and considering also co-linear compressive loads to the trusses according to director angles, the parallel load $F_\parallel$ is equal in modulus to F_{rodR} when the collapse strength of the base material is reached. Consequently, combining Eq. (11) and Eq. (5), the core compressive strength considering unit cell member fracture, is obtained by Eq. (12).

$$\sigma_{cR} \approx \frac{R_{1s}^-\pi d^2}{2l^2\cos^2\omega\sin 2\alpha}\sin\omega \qquad (12)$$

3.2.1.3. Analytical results. The analytical predictions of the failure modes are plotted in Fig. 8, identifying Euler buckling failure mode (σ_{cB}) as the blue-dashed curve (calculated using Eq. 10); and rod fracture (σ_{cR}) as the green-dotted-dashed curve (Eq. 12). The dominant modes are plotted as the dark-green region, or the area below the curves for the minimum compressive stresses.

The strengths predictions for the analyzed cases are exhibited in Table 4. Therefore, the predicted modes are buckling failure for the 0.5

Table 4
Core compressive strengths by analytical approaches. (*) Calculated using $k = 0.7$.

Ø [mm]	L [mm]	H [mm]	α [°]	ω [°]	$R_{\overline{1}s}$ [MPa]	E_{rod1s} [MPa]	σ_{cB}* [MPa]	σ_{cR} [MPa]
0.50	17.96	25.40	45	45	450	115	0.193	0.775
1	17.96	25.40	45	45	450	115	3.098	3.106
1.50	17.96	25.40	45	45	450	115	15.72	7.009

Table 5
Core compressive strength due to Euler buckling for different k coefficients.

Ø [mm]	$k = 0.5$ σ_{cB} [MPa]	$k = 0.6$ σ_{cB} [MPa]	$k = 0.7$ σ_{cB} [MPa]	$k = 0.8$ σ_{cB} [MPa]	$k = 0.9$ σ_{cB} [MPa]	$k = 1$ σ_{cB} [MPa]
0.5	0.379	0.263	0.193	0.148	0.117	0.095
1	6.072	4.216	3.098	2.372	1.874	1.518
1.5	30.827	21.407	15.728	12.042	9.514	7.707

mm and 1 mm rod cores, even though the latter are also found closer to the fracture region, and fracture regarding the 1.5 mm rod cores.

A seed value $k = 0.7$ is employed for the buckling calculations (Eq. (9)). Nevertheless, different attainable strengths while varying k coefficients are presented in Table 5 as an example of the attainable strength values for the core cases analyzed. The k coefficients may be calculated indirectly via numerical and experimental data.

3.2.2. Numerical approach

The FE simulations give support to the analytical models by evaluating the failure independently via two different approaches: Linear static simulations for the strength case (where rod buckling is not allowed), and non-linear simulations for the stability case (where rod buckling is allowed).

3.2.2.1. Linear static simulations. The core elastic modulus and the local stresses of the rods are predicted within this section. The case of 0.5 mm is presented as a study example for the procedure, although the results are then given for each rod case. The model is referred to Fig. 5 case. It shall be mentioned that the simulated stress shown is only hypothetical, noting that the maximum strength without buckling of the bars is 450 MPa (Table 1).

Fig. 9 presents renderings of the bending moments and combined stress distribution. The force is then mostly transferred as axial compressive loads to the rods, throughout the director angles ω and α. The axial load has a value of 353.35N per rod and represents more than 99 % of the stress components. Contrasted with theory, the peak value is on average $\sigma_s = \frac{1}{4} \frac{1000}{\sin 45} / \pi \frac{0.5^2}{4} = 1800.63$ MPa, having good correspondence with the simulations. The bending moment, although almost negligible, results in a linear distribution with a maximum at both the rod's ends and at the mid-plane due to the applied constraints. The fact of neglecting the transverse term in the calculations (see Appendix) is supported as well due to the predominance of the axial load calculated. The core cases for 1 mm and 1.5 mm rods presented similar results, with the same axial loads along the rods, although attaining an average of axial simulated stresses of 449.89 MPa and 199.95 MPa, respectively.

3.2.2.2. Non-linear simulations. The non-linear simulations show the critical instability load attainable for each core case. The simulation is carried out by applying vertical loads over the top nodes, at the same time acquiring the displacements performed by the rest of the nodes, until the model becomes unstable, and the simulation stops. Thus, tracking points on selected representative nodes are extracted and their trajectory curves are given in Fig. 10, starting from zero displacement up to instability, while reaching the critical load. The displacement of the nodes denotes an asymptotic distribution to which is possible to identify the critical applied load and indirectly obtain the approximated critical factor k given by Eq.(8). The critical loads P_{crit}^* are found at 60.6 N, 862.5 N and 3865.6 N for diameters 0.5 mm, 1 mm, and 1.5 mm, respectively.

Furthermore, the material distortion due to the applied load in the instability step is provided in Fig. 11. Remarkably, the sketches present a change in the orientation at the mid-section, denoting a rotation at the inflection point as the effect of the simultaneous buckling of the rods (here, the node is freed to rotate). It could be inferred that the constraint of the rotating mid-node does not have any influence on the vertical displacements according to the linear simulations, but it can play a fundamental role when evaluating the buckling of bars. In practical terms, as an example, if Euler's critical factor k might vary from ≈ 0.7 to 0.5, the critical load of the proposed real cases would be underestimated. This study is out of the scope of this work.

3.2.2.3. Simulations results. Table 6 shows a summary of the predicted strength results. The core strength predictions exhibit a direct
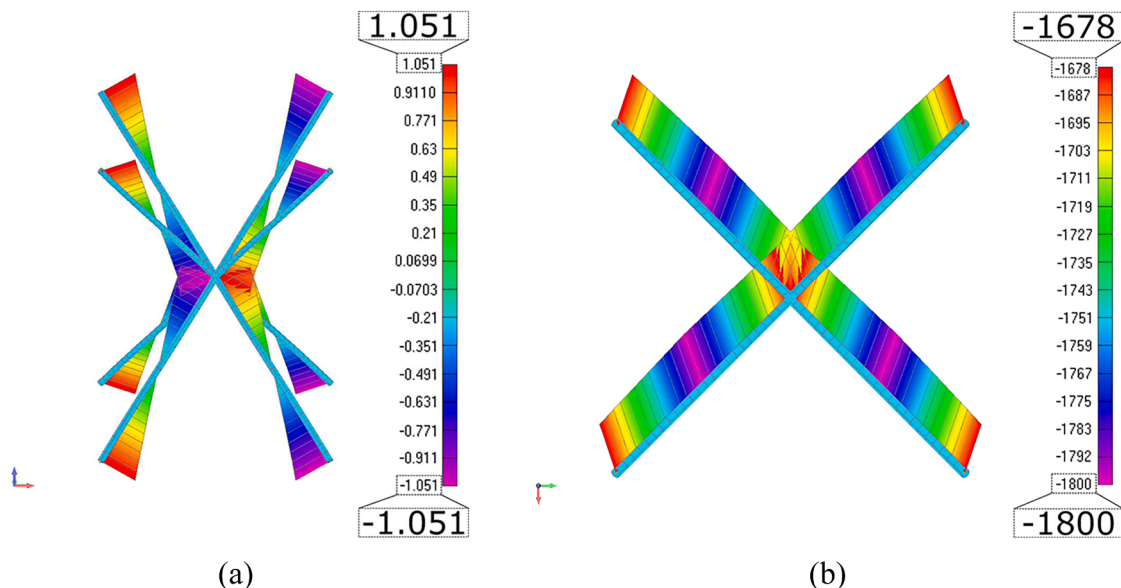

Fig. 9. FE-results due to compressive loads for the 0.5 mm rod diameter lattice unit cell. (a) Bending moments in [Nm]. (b) Combined stress distribution in [MPa].
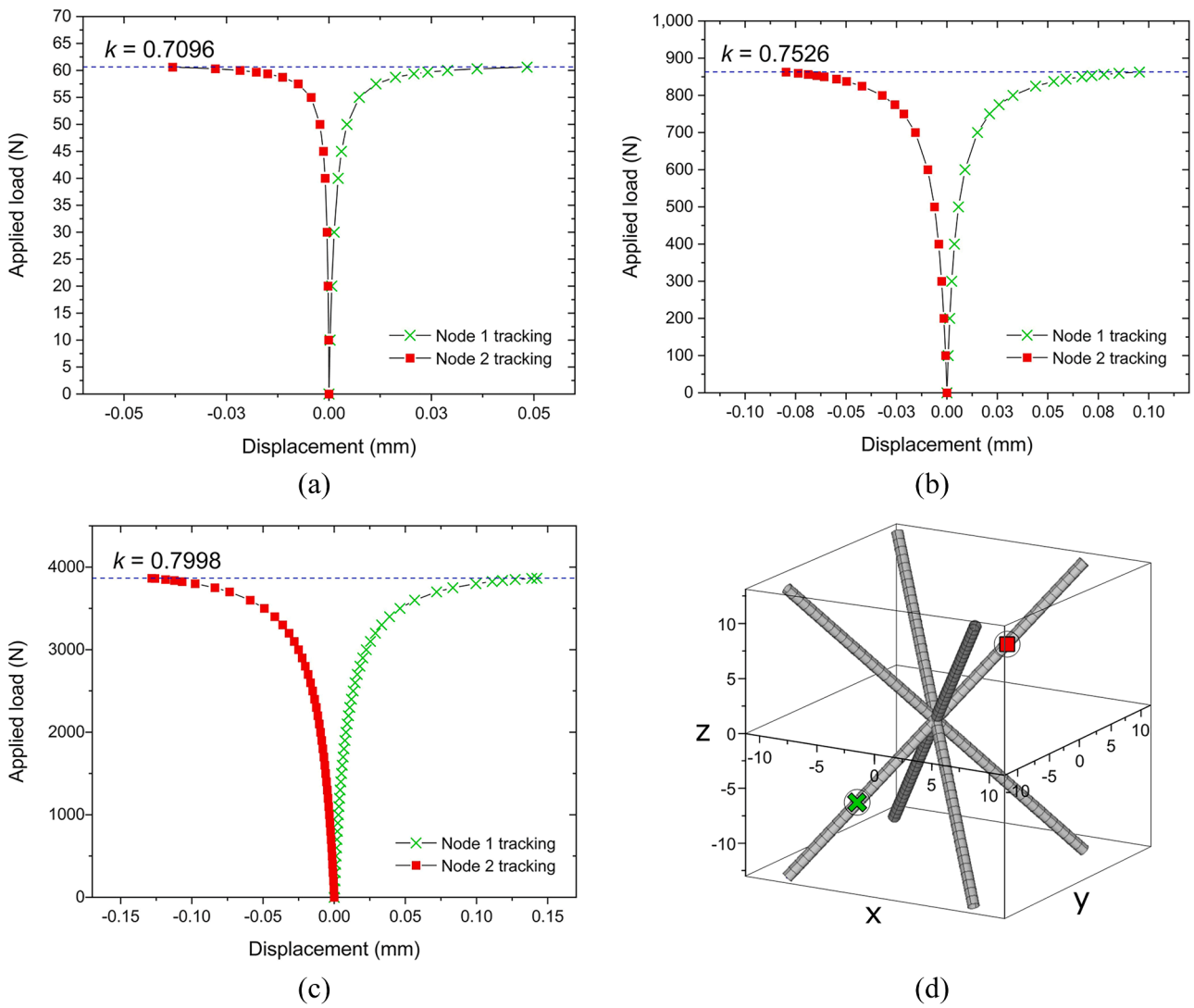
Fig. 10. Load vs. node displacement curves obtained from the non-linear simulations. (a) Ø = 0.5 mm. (b) Ø = 1 mm. (c) Ø = 1.5 mm. (d) Reference on node tracking.

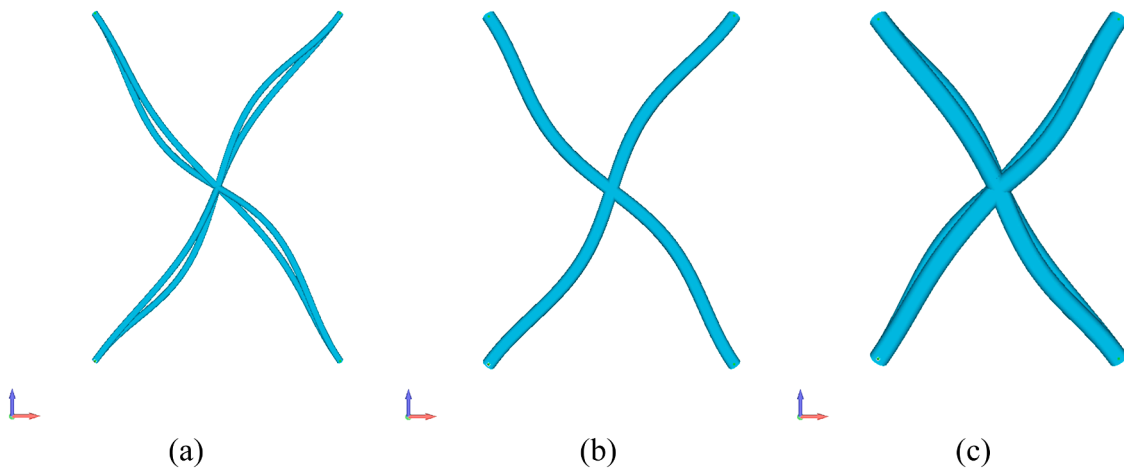**Fig. 11.** Renders obtained from FE buckling simulations at the failure step for different rod diameters, while compression loading. (a) Ø = 0.5 mm (front). (b) Ø = 1 mm (front). (c) Ø = 1.5 mm (front).

Table 6
Core compressive strengths from numerical and analytical approaches. (*) Non-linear static simulation. (**) Linear static simulation. (***) Analytical value. (‡) Calculated using $k = 0.7$.

Ø [mm]	L [mm]	P_{crit}* [kN]	σ_c* [MPa]	σ_c** [MPa]	σ_c*** [MPa]	Expected failure mode
0.50	17.96	60.6	0.187	0.775	0.193‡	Euler buckling
1	17.96	862.5	2.67	3.101	3.098‡	Euler buckling
1.50	17.96	3865.6	11.98	6.981	7.009	Fracture

dependence upon the rod's diameter size, i.e., the larger the rod diameter size, the higher the core strength. Thus, the expected core strengths are of 0.187MPa, 2.67MPa, and 6.981MPa (i.e., the minimum strength value for each case). The numerical results are in good correspondence with the theoretical values. The minimum strength is attributed to buckling failure for the slender rods (0.5mm and 1mm). In contrast, the rod diameter of 1.5mm may fail by fracture because of its larger rigidity as $E_{1s}.I_{x'}$

4. Experimental results

### 4.1. Compressive test procedure

Mechanical properties of the proposed lattice-based cores were evaluated following the ASTM C365 standard [2]. A Zwick / Roell Z150 screw-driven universal testing machine was employed for testing at controlled room temperature. Two displacement transducers type HBM W5TK were used for compensating potential misalignment of the samples to the compression plates. The cross-head speed was set to 0.5 mm/min. Three specimens of each core type were tested.

4.2. Compressive test results

The first case analyzed comprises the 0.5 mm rod cores (Fig. 12a). At the beginning of the test, the core shows a linear response followed by small changes in the slope, denoting a non-uniform load distribution. Little defects on the sample are visible, for example, as misalignment (Fig. 12b) which may cause small drops in the elastic modulus (point II),
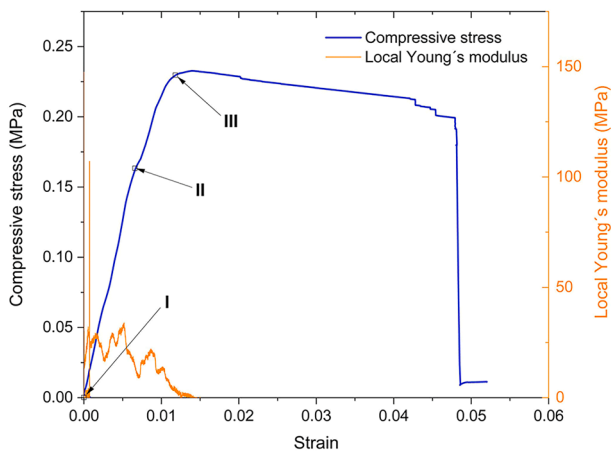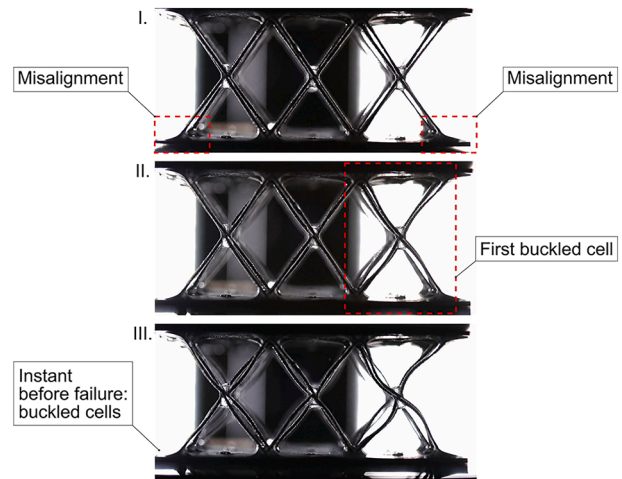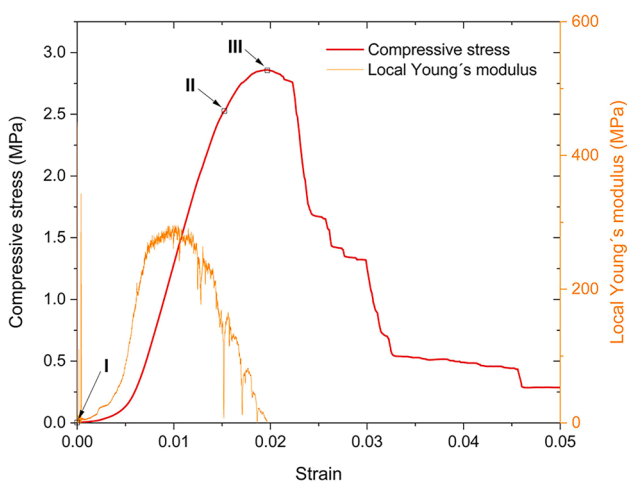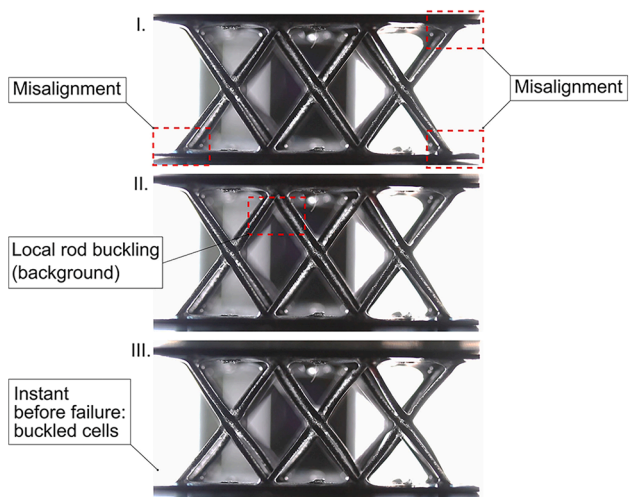

(a)　　　　　　　　　　　　　(b)

Fig. 12. Compressive stress-strain response of lattice-based core with Ø = 0.5 mm rods. (a) Compressive stress-strain curve. (b) Photographs associated to selected points.

(a)　　　　　　　　　　　　　(b)

Fig. 13. Compressive stress-strain response of lattice-based core with Ø = 1 mm rods. (a) Compressive stress-strain curve. (b) Photographs associated to selected points.

Fig. 14. Compressive stress-strain response of lattice-based core with Ø = 1.5 mm rods. (a) Compressive stress-strain curve. (b) Photographs associated to selected points.
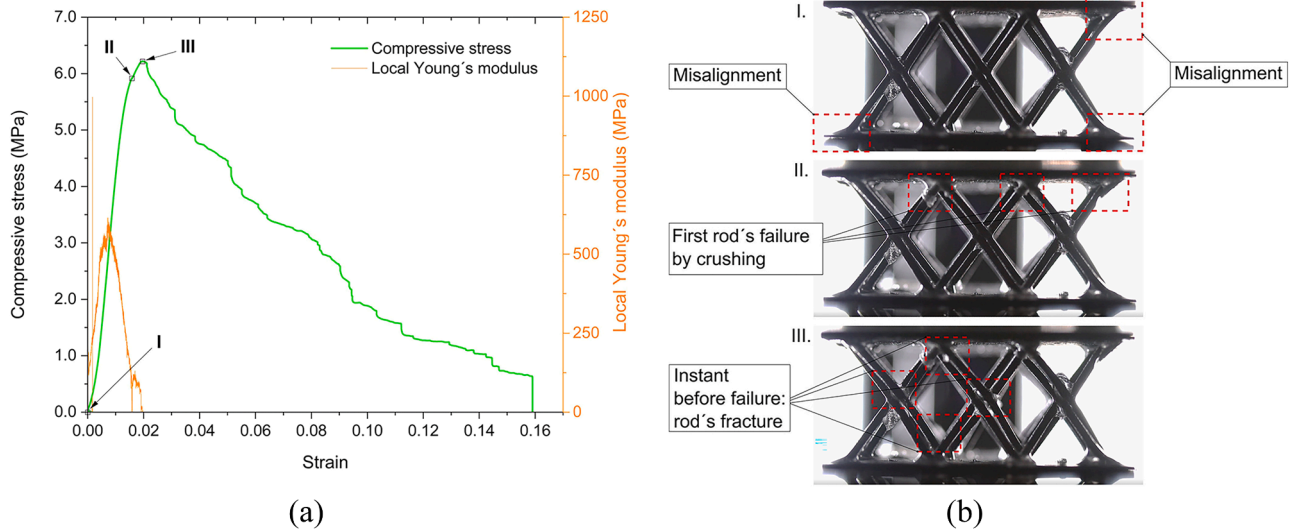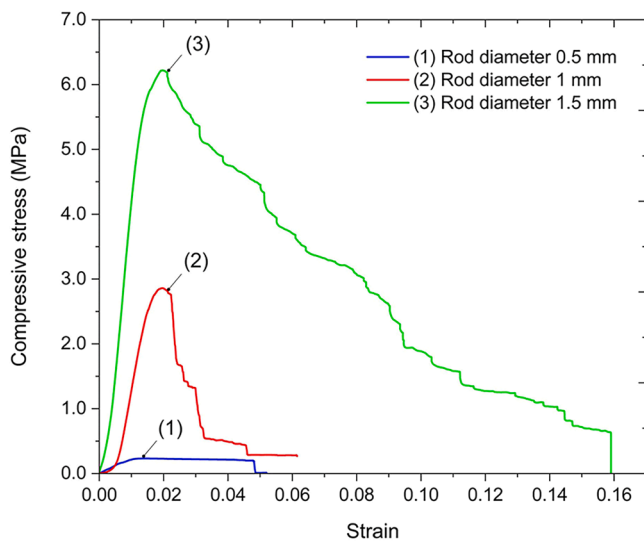

Fig. 15. Compressive stress-strain response of lattice-based cores.

negatively affecting the overall performance of the core, due to over-loading of the remaining rods and possibly subjecting them to local buckling. The failure step is reached at point III, where elastic buckling is the dominant mode. This observation is also supported by the fact that the load does not drop suddenly, but gradually with a sustained negative slope and a large straining until reaching the ultimate strain and failing afterwards.

The case 1 mm rod case is shown in Fig. 13. A linear region is seen as the load reaches point II. Local failure in the form of Euler buckling is observed upon this point (Fig. 13a), also detected as the evident local

drop in the elastic modulus. After point II, the load continues to increase at a smaller rate until it tops out at point III, where photographs give evidence of the rod's buckling (Fig. 13b). The collapse of the structure develops subsequently going over to a negative stress slope which maintains upon the straining until reaching its maximum deformation.

The last case for 1.5 mm rod cores (Fig. 14a) presents an evident Hookean region at the beginning of loading, until point II. At this point, the sudden drop in the elastic modulus and the local variation of the load curve indicates local failures, and in this case, in the form of a rod's fracture (Fig. 14b). After point II, the increase of the stress carries over to its maximum at point III, after which the structure collapses due to the rod's crushing. After failure, the stress curve steps down continuously over the strain until the end of the test.

The compressive stress vs. strain charts for the best-performed cores are presented in Fig. 15. The difference among the curves is evident regarding the strength values and shape as a result of a larger rod's cross-sectional area and the rod's rigidity. The maximum strengths obtained are 0.24 MPa, 2.88 MPa, and 6.23 MPa for rods' diameters varying 0.5 mm, 1 mm, and 1.5 mm, respectively. The smaller diameters exhibited a similar response after topping out the maximum value, both showing a sustained straining although with a negative slope, until the collapse of the structure. In contrast, the 1.5 mm case showed a sudden drop in stress after its maximum, and a continuous failure of the material as it was compressed until the end of the test.

5. Discussion

The analytical and FE models presented a successful correlation with the experimental tests as foreseen (Table 6). The failure is then attained by the mechanism that demands the lowest load to appear. A comparison of the predicted values and those obtained from the compressive tests is presented in Table 7. The analytical models for the buckling study took a seed value $k = 0.7$ so that very small discrepancies from the

Table 7
Analytical, FE, and experimental results from compressive tests.

Ø	Analytical		Numerical		Experimental		
	σ_{cpk}	E_c	σ_{cpk}	E_c	σ_{cpk}	E_c	Observed failure
[mm]	[MPa]	[MPa]	[MPa]	[MPa]	[MPa]	[MPa]	mode
0.5	0.193	99.05	0.187	100.65	0.22 ± 0.006	33.91 ± 3.96	Euler buckling
1	3.098	396.89	2.67	403.95	2.87 ± 0.011	267.8 ± 17.83	Euler buckling
1.5	7.009	895.59	6.981	909.19	5.87 ± 0.314	472.55 ± 119.04	Fracture
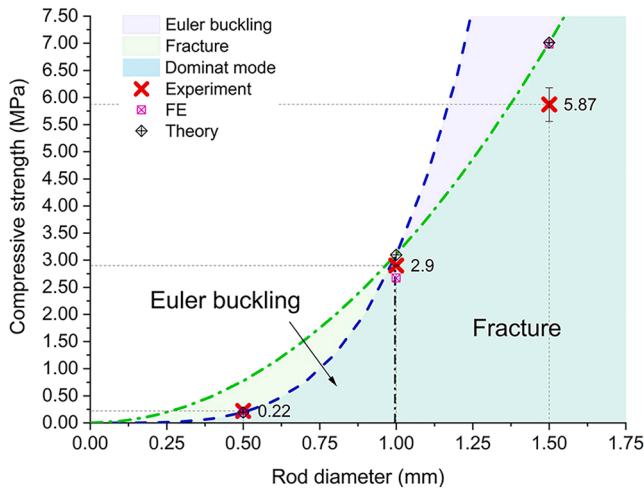
Fig. 16. Resulting failure maps: theoretical, numerical, and experimental data.

Fig. 17. Comparison of different performance indexes in compression of similar cores.

numerical value occur. By adjusting the k-values gained from the simulations, the analytical models could be further accurate to the experimental results. For example, employing $k = 0.753$ (Fig. 10b) in Eq. 9 for a 1 mm rod size, the analytical strength σ_{cpk} turns 2.68 MPa closer to the numerical result seen in Table 7. Additionally, the rod deformation seen in the FE (Fig. 11) showed a rotation of the mid-plane connecting node, as a consequence of the rod deformation and the free rotational border condition assigned. Seeing that the rods failed at the same time, the authors disregard a connection between a premature failure of one rod that may trigger the bucking of the rest cell members. Nevertheless, the experiments have shown that at the beginning of buckling (point II in Fig. 14b) some rods buckle just an instant before the others. Hence, further buckling studies with induced failure in FE are recommended to be carried out.

Additionally, the models correctly predicted the failure modes and peak strength. The predicted failure modes, such as Euler buckling and Fracture, can be further observed in Figs. 12a–14a at an instant before failure. In addition to the photographs, the type of failure mode can be inferred from the curves. In the case of the 0.5 mm and 1 mm rods, a typical buckling behavior is observed, where the load-displacement relationship is almost linear until a critical load is reached. Then continuing with a stable non-linear behavior until reaching a maximum deformation and instability, where the sample fails catastrophically. Given the slenderness of the 0.5 mm rods, after the critical buckling stress (approx. 0.2 MPa) the deformation relative to the applied load is much higher than in the 1 mm case since the latter has a higher stiffness due to the increased diameter. On the contrary, the failure of the 1.5 mm rods is evidenced as a fracture. The theoretical buckling load is almost twice as high as the fracture load (Table 4) due to the higher stiffness provided by the larger diameter. Fig. 14a shows that once a maximum stress is reached, the load-displacement relationship is not stable but the material fails and the stress drops, albeit gradually.

Seeing the elastic moduli, the standard deviations are relatively high. This suggests defects (manufacturing induced, test setup, etc.) causing a misdistribution of the loads in which some of the cells were overloaded than others (i.e., non-equally supported load), presumably by the misalignment of the skins concerning the compression plates (Figs. 12b–14b). These misalignments mean that the rods are not ideally at 45° at the beginning of the test, as ideally thought in the models, thus, the experimentally attained modulus (measured at the beginning of the test [2]) is lower than the predicted. However, the predicted compressive strength has a smaller discrepancy about the experiments suggesting that the load is better distributed over the specimen near the end of the test. This could be confirmed by tracking the angle of the rods at each time step while performing image analysis over new experiments.
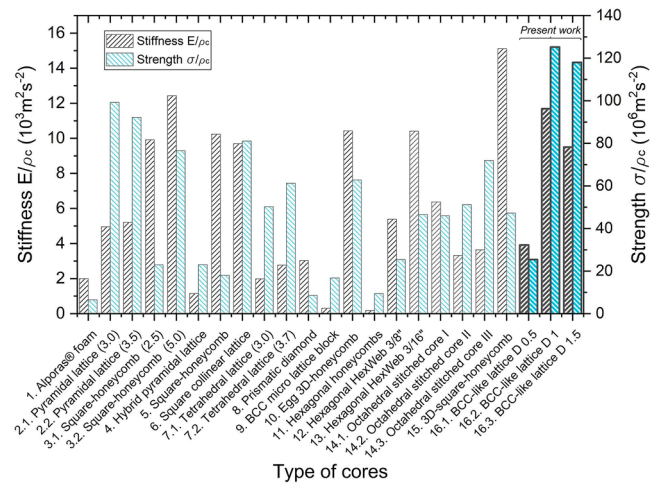
Table 7 is complemented by Fig. 16. The experimentally attained strengths are expressed as the x-dots upon each rod case. The 0.5 mm rod case lay directly over the buckling predicted region with excellent correspondence. In particular, according to the theoretical model representation, the case for 1 mm rods set down a point over a frontier between failure zones, and thus, it could present either failure due to buckling, fracture, or mixed. Further, referring to its experimental and numerical data, the acting failure mode is attributed to Euler buckling. Last, the 1.5 mm rods are set in the fracture area of the maps, with a very good correlation (near 10 % deviation).

6. Comparison with similar materials

The experimental results (mean values) obtained in this work are compared with those reported in the literature in Fig. 17 and complemented by Table 8. The compressive properties of different cores or geometries commonly used in sandwich structures such as lattices, honeycombs, and foams, are shown. The comparison with other bulk materials is made in a specific way, that is, regardless of their density. This compares the efficiency of a selected material for a lightweight application. The indexes of performance as E_{3c}/ρ_c and σ_{3c}/ρ_c are taken as comparison factors. Emphasis is put on ultra-lightweight cores.

In this work, the BCC-like lattice cores have compression ratios ranging from $3.91 \times 10^3 m^2 s^{-2}$ to $11.68 \times 10^3 m^2 s^{-2}$ and from $25.4 \times 10^6 m^2 s^{-2}$ to $125.2 \times 10^6 m^2 s^{-2}$, in terms of specific modulus and specific strength, respectively. In Fig. 17, the specific modulus of the rod diameter d = 1mm (Nr. 16.2) outperforms all the cores assessed, except for the Nr. 3.2 and Nr. 15 CFRP square honeycomb types, showing differences of about $0.75 \times 10^3 m^2 s^{-2}$ and $3.43 \times 10^3 m^2 s^{-2}$ respectively. In general, plate-based cores present a higher modulus than rod-based or foam-based materials of the same density [29]. Nevertheless, the specific strength of the lattice with $d = 1$ mm (Nr. 16.2) and $d = 1.5$mm (Nr. 16.3) reach higher strength indexes than all similar cores found in the literature known to the authors. For instance, the rod diameter $d = 1$mm (Nr. 16.2) exceeds the best-found cores as lattice-type Nr. 2.1 by ≈ 21 %, and honeycomb type Nr. 3.2 by ≈ 39 %. Additionally, observing Table 8 and comparing the performances of very similar cores such as the octahedral stitched cores (Nr. 14.2) of almost the same densities (ca. 22 kgm^{-3}), it is noticed that the proposed lattice cores Nr. 16.2 shows better compression stiffness (≈ 74 %) and strength (≈ 60 %), reflecting the importance of manufacturing CFRP-based lattices with straight and not curved elongated members [4]. Furthermore, regarding design engineering, it is useful to compare the core performance directly with standard commercial materials such as aluminum-based honeycomb

Table 8

Comparison of similar core materials in compression loading.

Nr. [–]	Type of cores [–]	Base material [–]	ρ_c [kgm^{-3}]	$\bar{\rho}^*$ [%]	E_c [MPa]	σ_c [MPa]	Reference [–]
1	*Alporas® foam*	Aluminium closed cell	200	8.0	400	1.3	Ashby et al. [1]
2.1	Pyramidal truss lattice	Laminate [0/90]°CFRP	43.2	3.0	214.27	4.28	Finnegan et al. [9]
2.2			50.4	3.5	262.58	4.65	
3.1	Square-honeycomb	Woven [0/90]°CFRP	34.25	2.5	339.76	0.79	Rusell et al. [22]
3.2			68.5	5.0	851.45	5.24	
4	Hybrid pyramidal lattice	Braided CFRP	43.5	3.0	50.7	1.00	George et al. [10]
5	Square-honeycomb	AISI 304	239.4	3.0	2449.06	4.33	Coté et al. [6]
6	Square collinear truss lattice	Ti–6Al–4V-coated SiC	377.28	9.6	3659.62	30.6	Moongkhamklang et al. [19]
7.1	Tetrahedral truss lattice	Age-hardened AA 6061	81	3.0	161.19	4.06	Kooistra et al. [14]
7.2			99.9	3.7	276.72	6.12	
8	Prismatic diamond	AISI 304	287.28	3.6	870.46	2.46	Coté et al. [7]
9	BCC micro lattice block	EOS Ti6Al4V	246.96	5.6	76.56	4.14	Crupi et al. [5]
10	Egg honeycomb grid panel	Laminate [0/90]°CFRP	46.5	3.0	485	2.92	Xiong et al. [36]
11	Hexagonal honeycombs	Woven Kevlar/914	57.96	4.2	10.43	0.55	Hou et al. [13]
12	Hexagonal HexWeb® (3/8",.001 unit-cell)	Aluminium 5052	25.6	1.02	137.89	0.65	Hexcel corp. [12]
13	Hexagonal HexWeb® (3/16",.001 unit-cell)	Aluminium 5052	49.65	1.99	517	2.31	Hexcel corp. [12]
14.1	Octahedral stitched core	Stitched	7.17	0.75	45.8	0.33	Che et al. [4]
14.2		tow-preg CFRP	22.27	1.41	69.46	1.14	
14.3			35.71	2.26	129.85	2.57	
15	3D Square- honeycomb (design 1)	Woven [0/90]°CFRP (plates)	47.64	3.52	720	2.25	Vitale et al. [31]
16.1	BCC-like lattice cores	Uni-directional CFRP (pultruded rods)	8.66	0.58	33.91	0.22	*Present work*
16.2	(D 0.5, D 1, D 1.5)		22.92	1.53	267.8	2.87	
16.3			49.76	3.32	472.55	5.87	

Note: (*) Approximated values.

cores (Table 8). Aluminum honeycombs have been established for many years as extensively used sandwich cores for aircraft and automotive industries [33]. Then, considering the commercial core of density 25 kgm^{-3} Nr. 12 and comparing them with the proposed lattice counterpart Nr. 16.2, the latter nearly double their compressive elastic modulus and quadruplicate their compressive strength. For core densities near 48 kgm^{-3}, Nr. 13 the elastic moduli are almost of the same order as the proposed lattices Nr. 16.3 exhibiting an 8.6 % difference. In terms of strength, the proposed lattices Nr. 16.3 shows 2.5 times more compression strength than their aluminum equivalent Nr. 13.

7. Conclusions

The design of three different novel ultra-lightweight cores based on lattices was presented and their compressive behavior was studied via micro-mechanical models, numerical models, and tests. The study is limited to simple and conventional predicting models targeting first insights on the competitiveness of the core proposals and not a detailed failure evaluation, and at the same time giving feasibility to the manufacturing method. The peak compressive strength was predicted satisfactorily with a very good correlation between the proposed models and experimental results. The discrepancy detected is attributed to imperfections incorporated during the manufacturing or the test setup. Further analyses are suggested for evaluating the entire failure map regions, validating more accurate models and comprehensive failure behavior.

The observed failure modes are attributed to Euler buckling for the smaller diameters and fracture of the rods for the largest. As seen in the numerical models, little difference is in the displacement analysis either as a BCC or BCC-like structure. The members in a BCC-like structure do not have a common coincident point, which may affect the final stiffness of the rod's mid-plane in vertical and horizontal directions, and differ slightly for each rod's diameter case, as seen in the FE models (different k-values varying with the rod diameters). The rods with larger stiffnesses present a higher k-value. Hence, the elastic link in the mid-plane (connection point) would exert less influence on the rods on the vertical displacement. A way to accurate the simulations to evaluate the

stiffness effect of the linking is, for example, to provide torsion springs in the mid-plane node, which elastic spring constant could be obtained indirectly from the experiments. However, a good starting point was to assume an Euler factor k of ≈ 0.7 as seed value for the theoretical analysis of buckling failure.

This work further validates the competitiveness of BCC-like structures made from pultruded rods contrasted to other bulk materials intended for lightweight applications. The properties of composite materials are mainly defined by the amount of fiber volume content available: the more fiber content the better the mechanical properties, although up to a limit. During the fabrication, using prefabricated pultruded rods with 65 % fiber content allows working with almost the maximum volume content that could be advantageously employed [24]. Conventional VI-based manufacturing methods for impregnating fibers or dry preforms can achieve fiber content values from 34 % up to 52 % or 55 % [10,27].

Employing prefabricated pultruded rods is advantageous, since the rod's cross-section is almost a homogeneous circumference along the length of the member, avoiding non-uniform profiles as observed in braided or stitched ones [4]. A more circular cross-section CFRP truss is less susceptible to elastic buckling [10]. Although plate-based cores have a higher specific stiffness than rod-based, plate-based cores present a much lower specific maximum strength (Fig. 17). The lattices based on rods have a good combination of stiffness and compressive strength.

Another advantage of the fabrication method lies in the vacuum-assisted resin infusion process used to interconnect the rod members in the sacrificial support structure. The resin is infused into the mold, not to impregnate the rods, since they are already resin-impregnated and cured, but allowing the resin to solidify, while keeping the rods at a specific orientation angle. Thus, controlling the right rod position is crucial to transfer the loads axially with the least flexural moment as possible (see Fig. 9), which may lead to premature stabilization failure or unexpected additional flexural stresses.

Another aspect worth mentioning is that the diameter of the rods does not directly influence the compressive performance of the cores. Absolute properties improve while increasing the rod diameter, for example by changing the failure mode from buckling to fracture.
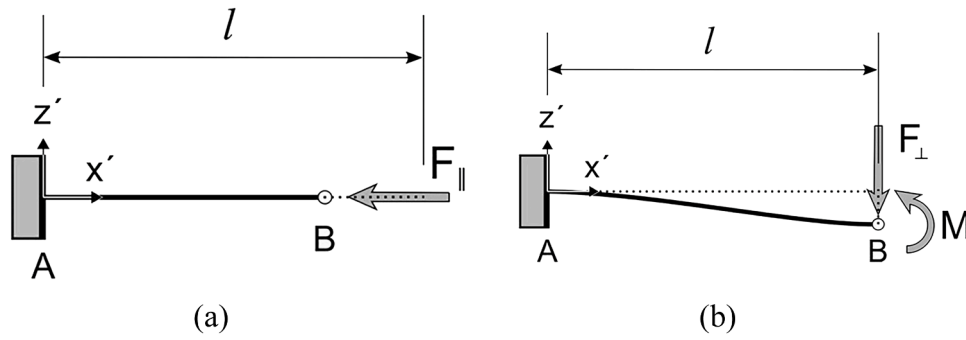
Fig. 18. Schemes of a cantilever beam. (a) With an axial load. (b) With a guided end.

However, specific properties show that, for instance, 1 mm rods are more efficient than 1.5 mm rods in resisting the compressive load intended for a very low weight application (Fig. 17). Therefore, increasing the rod diameter also increases the core density, negatively affecting the performance index.

Hence, the manufacturing method and the base material selection overcome the disadvantages involved in other similar bulk structures as mentioned above. The proposed cores showed an enhanced mechanical performance, exceeding the specific compressive properties of most materials known in the literature.

CRediT authorship contribution statement

Pablo Vitale: Writing – original draft, Visualization, Validation, Project administration, Methodology, Investigation, Formal analysis, Conceptualization. **Joaquin Montero:** Writing – review & editing, Visualization, Methodology, Formal analysis. **Gaston Francucci:** Writing – review & editing, Supervision, Methodology, Formal analysis. **Helmut Rapp:** Writing – review & editing, Supervision, Resources, Methodology, Funding acquisition, Formal analysis, Conceptualization. **Kristin Paetzold:** Software, Resources. **Ariel Stocchi:** Writing – review

& editing, Supervision, Formal analysis, Conceptualization. **Philipp Höfer:** Writing – review & editing, Validation, Resources, Funding acquisition, Formal analysis.

Declaration of competing interest

The authors declare that they have no known competing financial interests or personal relationships that could have appeared to influence the work reported in this paper.

Data availability

Data will be made available on request.

A. Appendix

Considering small displacements, when a beam is loaded by a concentrated load, the deflection δ_j at the loading point can be determined by calculating the partial derivative of the strain energy of the beam U concerning the acting forces Fj as Castigliano's second theorem as Eq. (A.1) [3,11].

$$\delta_j = \frac{\partial U}{\partial F_j} \tag{A.1}$$

In this way, based on the symmetry of the cell the model is sketched as a cantilever beam with a punctual load *F* at the core mid-plane (Fig. 18a). The displacement δ due to the load *F* is then defined by its perpendicular displacement components in parallel ($\delta_\parallel$) and perpendicular ($\delta_\perp$) directions according to the rod orientation as Eq. (A.2) and Eq. (A.3).

$$\delta_\parallel = \delta\sin\omega \tag{A.2}$$

$$\delta_\perp = \delta\cos\omega \tag{A.3}$$

Considering the displacement on each perpendicular direction, the internal strain energy of the beam in parallel direction $U_\parallel$ is caused by the parallel component of the force *F*, equal in modulus to the reaction $F_\parallel$, and depends on the cross-sectional area of the rod as $A_{rod} = \frac{\pi d^2}{4}$

$$U_\parallel = \int_0^l \frac{N^2 dx'}{2E_{rod1s}A_{rod}} \tag{A.4}$$

Eq. (A.4) shows the internal strain energy over the parallel load component. Factor *N* represents the general expression of the applied axial forces while E_{rod1s} is the Young's modulus of the base material of the rod in the parallel direction.

$$\delta_\parallel = \frac{\partial U_\parallel}{\partial F_j} = \sum_{j=1}^m \left(\int_0^l \frac{N_j}{E_{rod1s}A_{rod}} \frac{\partial N_j}{\partial F_i} dx' \right) = \frac{F_\parallel l}{E_{rod1s}A_{rod}} \tag{A.5}$$

Then solving Eq. (A.4) deriving with respect to F, the displacement in parallel direction is shown as Eq. (A.5). In this case, *N* is equal to $F_\parallel$. The perpendicular case is schematically represented in Fig. 18b as a cantilever beam with a guided end, at which the angle of the cross-section does not

change (rotation restricted). This effect is represented by a concentrated moment at the end of the beam M acting in an opposite way to the displacement due to $F_\perp$. The internal strain energy of the rod in perpendicular direction $U_\perp$ is dependent on the perpendicular component of the force F as $F_\perp$, and the flexural rigidity $E_{rod1s}I_{x'}$ of the truss (Eq. A.6). Factor M represents the general expression of the acting bending moment. The transverse shear effect upon the shear strain energy is neglected in this formulation due to the slenderness of the truss (L $>>$ d) and the truss is assumed as a Euler-Bernoulli beam.

$$U_\perp = \int_0^l \frac{M^2 dx'}{2E_{rod1s}I_{x'}} \tag{A.6}$$

Deriving Eq. (A.6) with respect to F the component of the displacement in the perpendicular direction is presented as Eq. (A.7). Component $I_{x'}$ represents the cross-sectional second moment of area, where $I_{x'} = \frac{\pi d^4}{64}$.

$$\delta_\perp = \frac{\partial U_\perp}{\partial F_j} = \sum_{j=1}^m \left(\int_0^l \frac{M_j}{E_{rod1s}I_{x'}} \frac{\partial M_j}{\partial F_i} dx' \right) = \frac{F_\perp l^3}{3E_{rod1s}I_{x'}} - \frac{M_{(x')}l^2}{2E_{rod1s}I_{x'}} \tag{A.7}$$

Since the angle at point B does not change at the end of the beam where $M_{(x')}$ and $F_\perp$ act, the sum of the rotations must be zero. Therefore, the angles at point B are calculated via Eq. (A.8) applying Castigliano's second theorem for rotations at the location of the concentrated force and moment.

$$\theta = \frac{\partial U_\perp}{\partial M_j} = \sum_{j=1}^m \left(\int_0^l \frac{M_j}{E_{rod1s}I_{x'}} \frac{\partial M_j}{\partial M_i} dx' \right) = \frac{F_\perp l^2}{2E_{rod1s}I_{x'}} - \frac{M_{(x')}l}{E_{rod1s}I_{x'}} = 0 \tag{A.8}$$

From Eq. (A.8) and solving for the moment $M_{(x')}$, then Eq. (A.9) defines the relations between the force and the opposite moment.

$$M_{(x')} = \frac{F_\perp l}{2} \tag{A.9}$$

Replacing Eq. (A.8) in Eq. (A.7), the total displacement at point B is then defined by Eq. (A.10).

$$\delta_\perp = \frac{F_\perp l^3}{3E_{rod1s}I_{x'}} - \frac{F_\perp l^3}{4E_{rod1s}I_{x'}} = \frac{F_\perp l^3}{12E_{rod1s}I_{x'}} \tag{A.10}$$

The core effective modulus E_c is defined by the unit cell modulus as Eq. (A.11), as the ratio of the compressive stress σ_c to the compressive strain ε_c of the unit cell.

$$E_c = \frac{\sigma_c}{\varepsilon_c} \tag{A.11}$$

According to Fig. 5 (main text) coordinate system, ε_c is then defined by Eq. (A.12)

$$\varepsilon_c = \frac{(\delta_\parallel^2 + \delta_\perp^2)^{\frac{1}{2}}}{l\sin\omega} = \frac{\delta}{l\sin\omega} \tag{A.12}$$

Moreover, since each unit cell has four trusses, the total compressive stress over a unit cell is given as Eq. (A.13), (corresponding Eq. (5) in the main text) specifying force P by its components according to z-direction.

$$\sigma_c = \frac{P}{A_{cell}} \equiv \frac{2(|F_\parallel|\sin\omega + |F_\perp|\cos\omega)}{(l\cos\omega)^2 \sin 2\alpha} = E_{rod1s} \frac{\pi d^2 \delta}{2l^3 \cos^2\omega \sin 2\alpha} \left[\sin^2\omega + \frac{3}{4}\left(\frac{d}{l}\right)^2 \cos^2\omega \right] \tag{A.13}$$

Substituting Eq. (A.13) and Eq. (A.12) into Eq. (A.11) and solving for E_c, the core modulus is given by Eq. (A.14).

$$E_c = E_{rod1s} \frac{\pi d^2 \sin\omega}{2l^2 \cos^2\omega \sin 2\alpha} \left[\sin^2\omega + \underbrace{\frac{3}{4}\left(\frac{d}{l}\right)^2 \cos^2\omega}_{transversal\ term} \right] \tag{A.14}$$

The component called as "transversal term" in Eq. (A.14), only contributes from 0.02906 % to 0.26 % to the expression in brackets for the cases analyzed in this work, so it will be neglected to ease calculations, and thus, Eq. (A.15) (corresponding Eq. (6) in the main text) is assumed to hold.

$$E_c \approx E_{rod1s} \frac{\pi d^2 \sin^3\omega}{2l^2 \cos^2\omega \sin 2\alpha} \tag{A.15}$$

References

[1] M. Ashby, Metal Foams: a Design Guide, Butterworth-Heinemann, 2000.

[2] ASTM C365/C365M22 Standard Test Method for Flatwise Compressive Properties of Sandwich Cores. (American Society for Testing, 2022), https://www.astm.org/c0365c0365m22.html.

[3] A. Boresi, R. Schmidt, Advanced Mechanics of Materials, John Wiley & Sons, 2003.

[4] L. Che, G. Xu, T. Zeng, S. Cheng, X. Zhou, S. Yang, Compressive and shear characteristics of an octahedral stitched sandwich composite, Compos. Struct. 112 (2014) 179–187, 6, https://linkinghub.elsevier.com/retrieve/pii/S0263822314000701.

[5] V. Crupi, E. Kara, G. Epasto, E. Guglielmino, H. Aykul, Static behavior of lattice structures produced via direct metal laser sintering technology, Mater. Des. 135 (2017) 246–256, 12, https://linkinghub.elsevier.com/retrieve/pii/S0264127517308407.

[6] F. Côté, V. Deshpande, N. Fleck, A. Evans, The out-of-plane compressive behavior of metallic honeycombs, Mater. Sci. Eng.: A 380 (2004) 272–280, 8, https://linkinghub.elsevier.com/retrieve/pii/S0921509304003387.

[7] F. Côté, V. Deshpande, N. Fleck, A Evans, The compressive and shear responses of corrugated and diamond lattice materials, Int. J. Solid. Struct. 43 (2006)

6220–6242, 10, https://linkinghub.elsevier.com/retrieve/pii/S0020768 305004919.

[8] L. Dong, H. Wadley, Mechanical properties of carbon fiber composite octet-truss lattice structures, Compos. Sci. Technol. 119 (2015) 26–33, 11, https://linkinghub.elsevier.com/retrieve/pii/S0266353815300944.

[9] K. Finnegan, G. Kooistra, H. Wadley, V Deshpande, The compressive response of carbon fiber composite pyramidal truss sandwich cores, Int. J. Mater. Res. 98 (2007) 1264–1272, 12, https://www.degruyter.com/document/doi/10.3139/146.101594/.

[10] T. George, V. Deshpande, K. Sharp, H. Wadley, Hybrid core carbon fiber composite sandwich panels: Fabrication and mechanical response, Compos. Struct. 108 (2014) 696–710, 2, https://linkinghub.elsevier.com/retrieve/pii/S0263822 313005151.

[11] J. Gere, B. Goodno, Mechanics of Materials (2013). OCLC: ocn741541348.

[12] Hexcel HexWebTM Honeycomb Attributes and Properties A comprehensive guide to standard Hexcel honeycomb materials, configurations, and mechanical properties. (Hexcel Corporation, 1999), https://www.pccomposites.com/wp-content/uploads/2015/07/PCHC4-4TY4TDS.pdf.

[13] Y. Hou, R. Neville, F. Scarpa, C. Remillat, B. Gu, M. Ruzzene, Graded conventional-auxetic Kirigami sandwich structures: flatwise compression and edgewise loading, Compos. Part B: Eng. 59 (2014) 33–42, https://doi.org/10.1016/j%20.compositesb.2013.10.084, 3.

[14] G. Kooistra, H. Wadley, Lattice truss structures from expanded metal sheet, Mater. Des. 28 (2007) 507–514, https://doi.org/10.1016/j%20.matdes.2005.08.013, 1.

[15] W Liu, H Song, Z Wang, J Wang, C. Huang, Improving the mechanical performance of fused deposition modeling lattice structures by a snap-fitting method, Mater. Des. 181 (2019) 108065.

[16] R. Mines, S. Tsopanos, Y. Shen, R. Hasan, S. McKown, Drop weight impact behaviour of sandwich panels with metallic micro lattice cores, Int. J. Impact Eng. 60 (2013) 120–132, 10, https://linkinghub.elsevier.com/retrieve/pii/S0734743 X13000912.

[17] J. Montero, P. Vitale, Support Structure and Manufacturing Method for Joining Prefabricated Parts, 2022, 4, https://worldwide.espacenet.com/patent/search/family/072852401/publication/EP3981568A1.

[18] J. Montero, P. Vitale, S. Weber, M. Bleckmann, K. Paetzold, Indirect Additive Manufacturing of resin components using polyvinyl alcohol sacrificial moulds, Procedia CIRP 91 (2020) 388–395. https://linkinghub.elsevier.com/retrieve/pii /S2212827120308386.

[19] P. Moongkhamklang, D. Elzey, H. Wadley, Titanium matrix composite lattice structures, Compos. Part A: Appl. Sci. Manufact. 39 (2008) 176–187, 2, https://li nkinghub.elsevier.com/retrieve/pii/S1359835X07002564.

[20] NASA Game Changing Development Program, Ultra-Lightweight Core Materials for Efficient Load-Bearing Composite Sandwich Structures Appendix, NASA, 2014. https://nspires.nasaprs.com/external/viewrepositorydocument/cmdocumentid=4 37864/solicita-tionId=%7BDCBA89BB-80B3-7E64-E1D7F6A2718573CB%7D/vi ewSolicitationDocument=1/Game%20Changing%20Development%20 Program-UltralightweightCoreMaterialsFINAL-Appendix%20C1%20AMENDMENT %201.pdf.

[21] R&G Faserverbundwerkstoffe Resins - Epoxy resin - Epoxy resin L + Hardeners (laminating resin). (R & G, 2022), https://www.r-g.de/en/list/Resins/Epoxy-resin/Epoxy-resin-L-Hardeners-laminating-resin-.

[22] B. Russell, V. Deshpande, H Wadley, Quasistatic deformation and failure modes of composite square honeycombs, J. Mech. Mater. Struct. 3 (2008) 1315–1340, 9, http://msp.org/jomms/2008/3-7/p07.xhtml.

[23] Siemens FEMAP User Guide Version 11.3. (Siemens, 2016).

[24] H. Schürmann, Konstruieren mit Faser-Kunststoff-Verbunden, Springer, Berlin, 2005 (Chapter 6.1).

[25] Smith, M., Cantwell, W., Guan, Z., Tsopanos, S., Theobald, M., Nurick, G. & Langdon, G. The quasi-static and blast response of steel lattice structures. J. Sandwich Struct. Mater.. 13, 479-501 (2011,7), http://journals.sagepub.com/doi/10.1177/1099636210388983.

[26] M. Smith, Z. Guan, W. Cantwell, Finite element modelling of the compressive response of lattice structures manufactured using the selective laser melting technique, Int. J. Mech. Sci. 67 (2013) 28–41, 2, https://linkinghub.elsevier.com/retrieve/pii/S0020740312002639.

[27] C Sun, H Albustani, VA Phadnis, MN Saleh, WJ Cantwell, Z. Guan, Improving the structural integrity of foam-core sandwich composites using continuous carbon fiber stitching, Compos. Struct. 324 (2023) 117509.

[28] Swiss Composites Technical Datasheet: UD Carbon- Profile und Rohre. (Swiss Composites, 2022), https://www.swiss-composite.ch/pdf/t-carbon-profile.pdf.

[29] Tancogne-Dejean, T., Diamantopoulou, M., Gorji, M., Bonatti, C. & Mohr, D. 3D plate-lattices: an emerging class of low-density metamaterial exhibiting optimal isotropic stiffness. Adv. Mater.. 30, 1803334 (2018, 11), https://onlinelibrary.wiley.com/doi/10.1002/adma.201803334.

[30] Toray Torayca T300: Standard Modulus Carbon Fiber. (Toray Inc., 2018), https://www.toraycma.com/wp-content/uploads/T300-Technical-Data-Sheet-1.pdf.pdf.

[31] P. Vitale, G. Francucci, H. Rapp, A. Stocchi, Manufacturing and compressive response of ultra-lightweight CFRP cores, Compos. Struct. 194 (2018) 188–198, 6, https://linkinghub.elsevier.com/retrieve/pii/S0263822317333585.

[32] K. Wei, Q. Yang, B. Ling, H. Xie, Z. Qu, D. Fang, Mechanical responses of titanium 3D lattice structure manufactured by selective laser melting, Extrem. Mech. Lett. 23 (2018) 41–48, 9, https://linkinghub.elsevier.com/retrieve/pii /S2352431618301299.

[33] T. Wierzbicki, Crushing analysis of metal honeycombs, Int. J. Impact Eng. 1 (1983) 157–174, 1, https://linkinghub.elsevier.com/retrieve/pii/0734743X83900040.

[34] J. Xiong, L. Ma, S. Pan, L. Wu, J. Papadopoulos, A Vaziri, Shear and bending performance of carbon fiber composite sandwich panels with pyramidal truss cores, Acta Materialia 60 (2012) 1455–1466, 2, https://linkinghub.elsevier.com/retrieve/pii/S1359645411008184.

[35] J. Xiong, L. Ma, L. Wu, B. Wang, A Vaziri, Fabrication and crushing behavior of low-density carbon fiber composite pyramidal truss structures, Compos. Struct. 92 (2010) 2695–2702, 10, https://linkinghub.elsevier.com/retrieve/pii/S0263822 31000111X.

[36] J. Xiong, A. Vaziri, R. Ghosh, H. Hu, L. Ma, L. Wu, Compression behavior and energy absorption of carbon fiber reinforced composite sandwich panels made of three-dimensional honeycomb grid cores, Extrem. Mech. Lett. 7 (2016) 114–120, 6.

[37] X Zhang, Q Meng, K Zhang, R Zhu, Z Qu, Y Li, et al., 3D-printed bioinspired Al2O3/polyurea dual-phase architecture with high robustness, energy absorption, and cyclic life, Chem. Eng. J. 463 (2023) 142378.

[38] X Zhang, K Zhang, B Zhang, Y Li, R. He, Mechanical properties of additively-manufactured cellular ceramic structures: a comprehensive study, J. Adv. Ceram. 11 (2022) 1918–1931.